IEEE Open Journal of Instrumentation and Measurement

Received 7 July 2025; revised 11 August 2025; accepted 14 August 2025. Date of publication 5 September 2025; date of current version 25 September 2025.
The review of this paper was arranged by Associate Editor Mohammad Tayeb Al Qaseer.

Digital Object Identifier 10.1109/OJIM.2025.3604983

Multilevel Validation of Direct Sampling Time-Domain Measuring Receivers

IVAN STRUZHKO [1] (Member, IEEE), MARC GARCÍA-BERMÚDEZ [2,3], JORDI SOLÉ-LLOVERAS [2,3] (Member, IEEE), MANUEL AÑÓN-CANCELA [4], TOM HARTMAN [1] (Member, IEEE), MARCO A. AZPÚRUA [2,3] (Senior Member, IEEE), AND FRANK LEFERINK [1,5] (Fellow, IEEE)

[1]Department of EEMCS, University of Twente, 7522 NB Enschede, The Netherlands
[2]EMC Electromagnetic BCN S.L. (EMC Barcelona), 08034 Barcelona, Spain
[3]Departament d'Enginyeria Electrònica, Universitat Politècnica de Catalunya, 08034 Barcelona, Spain
[4]Área de Compatibilidad Electromagnética, Instituto Nacional de Técnica Aeroespacial Esteban Terradas, 28850 Madrid, Spain
[5]THALES Nederland B.V., 7554 RR Hengelo, The Netherlands

CORRESPONDING AUTHOR: I. STRUZHKO (e-mail: ivan.struzhko@utwente.nl)

This work was supported in part by the European Partnership on Metrology, co-financed from the European Union's Horizon Europe Research and Innovation Programme under Project 21NRM06 EMC-STD, and in part by the European Union's EU Framework Programme for Research and Innovation Horizon 2020 under the Marie Skłodowska-Curie Grant through Project ETUT under Agreement 955646.

ABSTRACT Although the time-domain approach to electromagnetic interference evaluation offers numerous advantages, including shorter test duration and multichannel acquisition, its practical adoption remains limited. This is mainly because existing standards, such as CISPR 16-1-1, do not explicitly address direct sampling time-domain measuring receivers or define specific calibration and validation procedures for them. While several studies have demonstrated successful use cases, a comprehensive validation of such systems has not yet been performed. This article presents multilevel experimental validations of time-domain measuring receivers, focusing on the direct sampling approach and oscilloscope-based implementations. First, meta-comparisons of FFT-based receivers are made using calibration data obtained from certificates of accredited laboratories. Then, controlled signal sources with known time and spectral characteristics are used to cross-check with different measuring receiver models. Finally, several instruments are benchmarked with respect to their standard detector outputs when measuring the emissions of a power converter while spread spectrum techniques are used. The results show good agreement between the measuring receivers in the time domain and the tested conventional receivers in the frequency domain within the standard error, even though the complexity of the measured signals is different.

INDEX TERMS Compliance, electromagnetic emissions, measuring receiver, time domain, validation.

I. INTRODUCTION

TWO APPROACHES are primarily employed regarding the electromagnetic emission measurement instruments according to the standard method [1]. The classical one uses receivers with superheterodyne architecture, which allows for a large dynamic range even at high frequencies due to its scalability. On the other hand, FFT-based receivers digitally process the time-domain emission data to obtain accurate spectrum estimates while accelerating the frequency scans and allowing for real-time measurements.

The frequency-swept approach used by superheterodyne receivers is intrinsically slow and unsuited for measuring short-time emission events and time-variant electromagnetic interference (EMI), leading to potential detection errors and underestimating actual disturbance levels. Some real examples of time-varying emissions sources include those arising from different operation modes, such as the acceleration and deceleration of electric motors [2], [3] or spread spectrum (SS)-based pulse width modulation (PWM) techniques used in modern switch mode power supplies [4].

© 2025 The Authors. This work is licensed under a Creative Commons Attribution 4.0 License.
For more information, see https://creativecommons.org/licenses/by/4.0/

The development of time-domain EMI measurement systems has transformed electromagnetic compatibility (EMC) testing, offering faster and more detailed signal analysis compared to conventional frequency-domain approaches. Important milestones in the development of the time-domain EMI measurement approach are indicated in Section II. Among the main advantages of time-domain receivers that have been recognized in recent studies are the following. First, they shorten the test duration by capturing all necessary data over a single operating cycle of the equipment under test (EUT) [5].

Moreover, implementing the time-domain EMI measurements approach can help overcome the challenges of in situ electromagnetic emissions assessments, as shown in [6] and [7] and facilitates synchronous multichannel acquisitions within a single system as demonstrated in [8] for the case of multiline conducted emissions tests, or in [9] and [10] where multiple antennas are used to measure H-Field and E-Field simultaneously. Furthermore, time-domain receivers enable spectrogram visualizations, aiding in EMI characterization and classification.

The advantages of the time-domain EMI measurement approach are driving its increasing adoption, but still, its integration into compliance testing remains challenging due to the lack of explicit standardization. For example, the CISPR 16-1-1 standard [1] covers FFT-based receivers in a broad manner; however, implementations based on direct sampling instruments are not explicitly mentioned. Also, the said standard only gathers requirements that are common for any measuring receiver architecture under a black-box approach. This means there are no specific calibration requirements for time-domain EMI receivers, and some controversy remains concerning different measuring receiver architectures providing nonidentical measurement results. Furthermore, only limited validation of these systems has been reported, often focusing on individual performance metrics rather than a comprehensive, multilevel assessment.

To bridge this gap, we present a multilevel validation approach that systematically evaluates direct sampling time-domain EMI receivers against industry-standard frequency-domain EMI receivers. Unlike previous studies, this article introduces a comprehensive validation strategy that includes the following stages: establishing a meta-analysis of calibration data to verify baseline accuracy, conducting controlled signal experiments to test time-domain EMI receiver performance across different CISPR frequency bands, and benchmarking real-world EMI measurements using complex load cases (e.g., dc/dc converters with spread spectrum techniques). Thus, validation is achieved by comparing FFT-based direct sampling receivers and other measurement receiver architectures in experiments organized at three levels of complexity. In this context, the complexity of the experiment is related to the number of parameters required to define the reference signal. It provides empirical evidence to support the inclusion of direct sampling EMI receivers in future EMC standardization efforts. In total, this work reports five experiments made by three independent groups and institutions and considers nine different measuring receiver models. By addressing these gaps, this work ensures the reliability of direct sampling EMI receivers and lays the foundation for their broader adoption in compliance testing and EMC research.

The remainder of this article is as follows. Section II presents a background on time-domain EMI measurements. Section III presents a detailed methodology for each experiment. Section IV then presents the results and analyzes the adequacy of using direct sampling measurement devices for EMI measurements. Finally, Section V discusses the overall result obtained from the research and presents a conclusion.

II. BACKGROUND

The time-domain EMI measurement techniques have evolved as a powerful alternative to traditional frequency-domain receivers, offering faster and more comprehensive analysis of electromagnetic emissions. While superheterodyne receivers have been widely used for compliance testing, their frequency-swept approach is slow and struggles with time-variant signals, making them less effective for modern electronic systems. The foundation for time-domain EMI measurements was laid in [11] and [12], where authors introduced direct sampling and digital processing to extract amplitude and phase information across the entire frequency band, enabling real-time EMI analysis. A milestone was the digital model for the quasi-peak detector presented in [13].

Subsequent research presented in [14] focused on achieving CISPR 16-1-1 compliance, particularly for high-frequency measurements above 1 GHz, demonstrating in [15] that time-domain EMI receivers could replace conventional EMI measurement systems, including the measurement of discontinuous disturbances in [16]. Later enhancements were reported in [17], including modifications to the hardware architecture to achieve lower noise levels, increased measurement bandwidth, and a maximum measurable frequency of up to 40 GHz.

The trend in FFT-based measuring receivers resulted in various commercial instruments capable of real-time performance with increasingly higher measurement bandwidth. Due to their characteristics, these instruments ultimately became high-end solutions. Additionally, the time-domain information has remained largely unexploited in such instruments, as EMC standards for emissions tests do not require it for compliance evaluation.

At that point, Azpúrua et al. began working on a software layer implementation of the CISPR 16-1-1 measuring receiver, which could be combined with multiple general-purpose sampling instruments. For their practicality and wide availability, oscilloscopes were extensively used as direct measuring instruments, and the acquired signals were processed using the methods described in [18]. The results demonstrated excellent performance and revealed new potential applications for the statistical analysis of

interferences presented in [19] and [20], as well as their decomposition into transient and continuous modes in [21]. Azpúrua et al. called their approach "full time-domain emission measurement systems" where the directly sampled waveform information is kept as an integral part of the measurement results and the utilization of time-domain data is conducted more broadly.

Advancements in oscilloscope technology and the affordability of direct sampling FFT-based receivers have made time-domain EMI measurements a powerful tool for tackling real-world EMI challenges. Researchers have demonstrated their effectiveness in multichannel, multitransducer setups for faster EMI analysis [22], improved detection of low-repetitiveness cyclo-stationary disturbances [23], and precise characterization of impulsive noise affecting energy meters [24]. In aerospace applications, time-domain methods have been used to analyze magnetic field emissions from reaction wheels [2], while their advantages for in situ EMI assessments in harsh environments have been highlighted in recent studies [6].

Assuring the quality and reproducibility of emissions measurement is mandatory in the context of compliance testing. Therefore, the appropriate performance must be guaranteed for direct sampling FFT-based measuring receivers. One way to approach this problem is through a traceable calibration, as with any type of measuring receiver. This is a problem explored in [26], and it is found that typical measuring receiver calibration procedures are nonoptimal for direct sampling implementations. In other papers, the measurement accuracy [26], [27] and dynamic performance [28] of full time-domain EMI measurement systems are evaluated. However, the lack of a benchmark comparing commercial solutions versus the direct-sampling implementations of FFT-based measuring receivers resulted in an information gap and speculation.

Given the many applications of direct sampling FFT-based measuring receivers explored in academia and research activities, their widespread acceptance and use could benefit from their clear coverage in EMC standards. To support the intended standardization work, on the one hand, the signal processing methods must be thoroughly explained and checked in a wide range of configurable parameters of the spectral estimation functions, as presented in [29] using systematic numerical experiments.

As a next step, this work tackled the empirical part of this endeavor, providing a robust validation scheme that follows a multilevel approach. It introduces a structured validation approach, systematically comparing direct sampling time-domain EMI receivers with commercial CISPR-compliant receivers through a multilevel benchmarking process. By providing empirical evidence supporting the accuracy, reliability, and standardization of time-domain EMI receivers, this work aims to facilitate their broader adoption in compliance testing and EMC research.

TABLE 1. Summary of the experiments.

Code	Experiment description	Team
E0	Meta-analysis of calibration data of EMI receivers using standard reference signals.	**A**
E1.1	Verifications using controlled modulated signals. Pulse modulated sinewave, CISPR bands B to D.	**A+B**
E1.2	Verifications using controlled modulated signals. Alternative signals, CISPR band A.	**C**
E2.1	Realistic emissions measurements using a commercial off-the-shelf (COST) DC/DC buck-boost converter.	**A+B**
E2.2	Realistic emissions measurements using a DC/DC GaN converter with alternative PWM.	**C**

TABLE 2. List of measuring receivers considered during the experiments.

ID	Measuring receivers	*E0*	*E1.1*	*E1.2*	*E2.1*	*E2.2*
R1	emiGO$^{(*,\triangle)}$ + R&S RTO64 DC - 3 GHz	✓	✓	-	✓	-
R2	emiGO$^{(*,\triangle)}$ + PS5444D DC - 200 MHz	✓	✓	✓	✓	✓
R3	R&S ESI$^{(\triangle)}$ (20 Hz - 40 GHz)	-	✓	-	-	-
R4	R&S ESW$^{(\triangle)}$ (1 Hz - 8 GHz)	-	✓	-	✓	-
R5	R&S ESW$^{(\triangle)}$ (1 Hz - 26.5 GHz)	✓	-	-	-	-
R6	R&S ESW$^{(\triangle)}$ (1 Hz - 44 GHz)	✓	-	-	-	-
R7	Keysight N9038B MXE $^{(\triangle)}$ (3 Hz - 44 GHz)	✓	-	-	-	
R8	R&S ESPI (9 kHz - 7 GHz)	-	-	✓	-	✓
R9	Signal Hound BB60C (9 kHz - 6 GHz)	-	-	✓	-	✓

NOTE: The instruments marked (*) are those based on direct sampling implementations. The symbol (△) highlights CISPR 16-1-1 compliance according to specifications, at least in the frequency range of the experiments.

III. METHODOLOGY

This section describes the measurement setups, procedures followed, and intended characteristics of the measured signals for each experiment. Experiments are arranged in the order of increasing complexity of the measured signal and identified through a code. The independent teams involved in each experiment are labeled as "**A**," "**B**," and "**C**" for INTA, EMC Barcelona, and the University of Twente, respectively. The summary of each experiment is given in Table 1 while the specific details are given in the following subsections.

This study considers various instruments from different manufacturers and architectures, as depicted in Table 2. To facilitate the presentation of the results, the EMI receivers in the selected sample have an associated identification code (ID). Receivers ID R1 and R2 are those based on direct sampling methods as described in [29]. It must be noted that all experiments use at least three different receivers, and the direct sampling approach is present in all experiments at least through one of the samples.

The selected instruments represent a cross section of measurement equipment commonly used in electromagnetic emissions testing, covering a range of receiver architectures (e.g., direct sampling and superheterodyne), brands, and typical performance classes. The comparison focuses primarily on amplitude-related parameters, such as deviations in measured signal levels and the behavior of standard detectors: peak (PK), quasi-peak (QP), and average (AVE), as defined in CISPR 16-1-1, since these are directly used in emissions compliance assessment. Their implementation

TABLE 3. E1.1—Signal characteristics.

Parameters	Value
Level (dBμV):	66
Tested frequency, (MHz):	1, 10, 100, 500
Pulse duration, τ (μs):	10, 20, 50
Pulse period, T (μs):	100, 1000

in the context of direct sampling receivers is discussed in detail in [29].

A. META-ANALYSIS OF CALIBRATION DATA

This experiment used calibration data extracted from certificates produced by ISO/IEC 17025 accredited laboratories. For calibration of measuring receivers, reference signals are typically sinewaves and baseband pulses. That means they have low complexity and are easily generated with lower measurement uncertainty in comparison to the signals used in the rest of the experiments. In particular, we focused on the baseline parameters required in [1]. All receivers are considered to comply with CISPR 16-1-1 according to their specifications. Calibration data confirmed this. However, we wanted to check how close direct sampling implementations performed with respect to the high-end receivers in these calibration conditions.

B. PULSE-MODULATED SINEWAVE

In this experiment, we measured pulse modulated sinewaves according to the characteristics defined in Table 3. The setup was configured with the output of the signal generator directly connected to the input of the measuring receiver. The source was a vector signal generator model Agilent E4438C (250 kHz–6 GHz). This signal allows for the verification and comparison of the response of the weighting detectors at a given frequency. Tested frequencies are found in CISPR bands B–D. This experiment follows a full factorial design, with a total of 90 measurements executed using the four distinct receivers considered.

C. ALTERNATIVE GENERATED SIGNALS

For the modulated signals in Table 4, this experiment evaluates the performance of measuring receivers within the CISPR band A. The test signals were chosen to comprise some of the characteristics of the emissions of power converters. Test signals E1.2.(1,2,3) have a constant frequency content while E1.2.(4,5,6) change their frequency content over the measurement time.

The test signals are generated by an arbitrary waveform generator (AWG) Teledyne T3AFG120. The measurement time is set to 100 ms to ensure an integer number of periods for all test signals. Then the measurement output of R2 and R9 are compared with R8 which is taken as the reference.

D. EMISSIONS OF COST DC/DC CONVERTER

The conducted emissions of the device reference AZDelivery XL-4016E1 are measured using the setup presented in

TABLE 4. E1.2—Test signal characteristics.

ID	Test signal	Parameters
E1.2.1	Sinewave	100 kHz, 1 V_{RMS}.
E1.2.2	Multitone	20/40/60/80/100/120/140 kHz, 100 mV_{RMS} each.
E1.2.3	Square pulse	20 kHz, 1 V_{PPK}.
E1.2.4	Chirp pulse	80 kHz - 120 kHz, 1 V_{RMS}, t_{spr} = 20 ms.
E1.2.5	Spread spectrum square signal	18 kHz - 22 kHz, 1 V_{PPK}, t_{spr} = 20 ms.

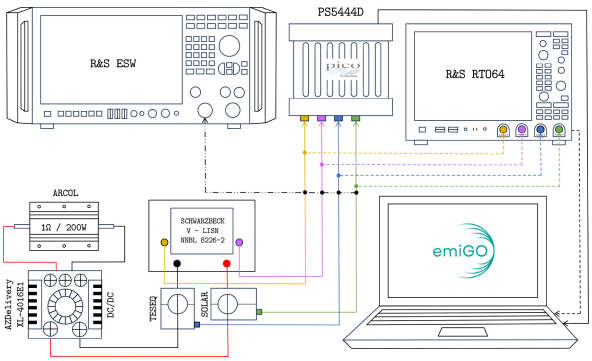


FIGURE 1. E2.1—The schematic of the measurement setup. Multichannel measurement is possible for R1 and R2. For R4, measurements are performed sequentially, one line at a time.

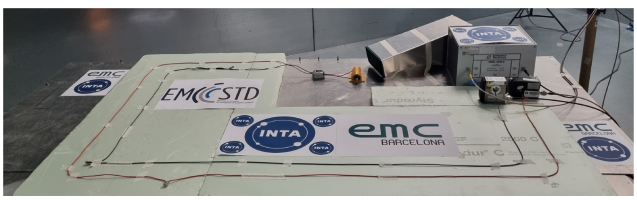


FIGURE 2. E2.1—The measurement setup.

Figs. 1 and 2. The device input voltage is set to 12 V, the output voltage is adjusted to 5 V, and the switching frequency is fixed at approximately 64 kHz. The device is loaded with a resistor (1 Ω–200 W). The transducer for measuring the disturbance voltage in the positive and negative input lines is a SCHWARZBECK V-LISN model NNBL 8226-2. The radiofrequency current is also measured in both lines using the probes MD 4070 (4 kHz–400 MHz) from TESEQ and 9250-1N (10 kHz–450 MHz) from Solar Electronics Company. The measurement parameters for R1, R2, R3, and R4 were set according to the MIL-STD-461G standard.

E. EMISSIONS OF DC/DC CONVERTER USING SPREAD SPECTRUM MODULATION

The conducted emissions of a CoolGaN 600-V half-bridge evaluation board are measured using the setup presented in Figs. 3 and 4. This device circuit is a buck converter based on Gallium Nitrate (GaN) transistors loaded with 8.2 Ω. This GaN converter is controlled by the development board LAUNCHXL-F28379D using MATLAB Simulink.

TABLE 5. E2.2—Spread spectrum modulation characteristics.

ID	PWM Type	Parameters
E2.2.1	Continuous	20 kHz, Steady
E2.2.2	Linear	18 kHz - 22 kHz, Period variation of 20 ms.
E2.2.3	Random	18 kHz - 22 kHz, Period variation of 20 ms.

[h]

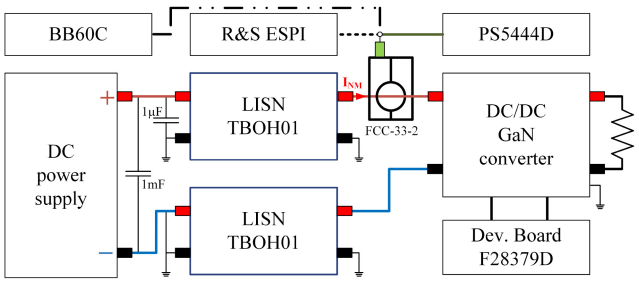


FIGURE 3. E2.2—The schematic of the measurement setup. The I_{NM} is measured via R2, R8, and R9 receivers.

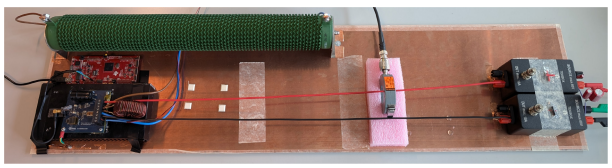


FIGURE 4. E2.2—The measurement setup.

Three types of switching frequency modulation are shown in Table 5. Two of them have been used to spread the spectrum of the emissions [4]. The GaN converter is supplied through the LISN model TEKBOX TBOH01 5 µH. The receivers used to measure the emission are R2, R8, and R9, as shown in Table 2. The RF current probe model F-33-2 (1 kHz–250 MHz) from the positive line measures the normal mode current (I_{NM}).

IV. RESULTS

In this section, the results of all experiments are presented in an orderly manner from E0 to E2.2. Due to page length constraints and for clarity reasons, only the most representative results are reported in what follows. The data of test conditions that have been omitted is available upon request.

A. META-ANALYSIS OF CALIBRATION DATA

The meta-analysis of the measuring receivers' calibration data is presented below. Due to the lack of standardization in the format for presenting such calibration results, most certificates reported the results differently. Therefore, the original data was normalized and plotted as in Figs. 5–8 to facilitate the necessary comparisons. The "upper" and "lower" limit lines in Figs. 5 and 6 correspond to the tolerances defined in CISPR 16-1-1 for the deviation of each of the compared parameters, based on calibration data.

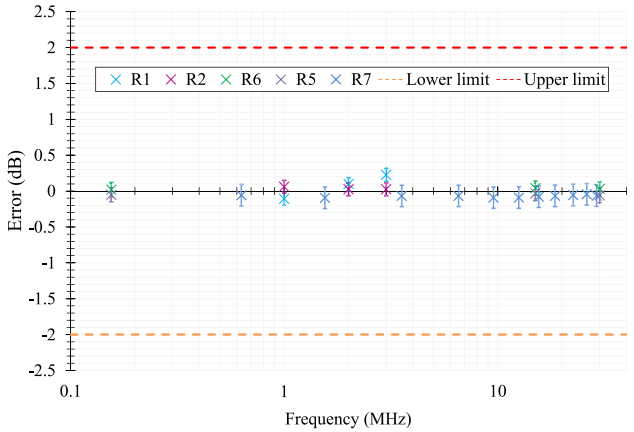


FIGURE 5. E0—CISPR Band B. Sinewave level accuracy calibration results. The frequency of the calibration points might be different for each receiver unit.

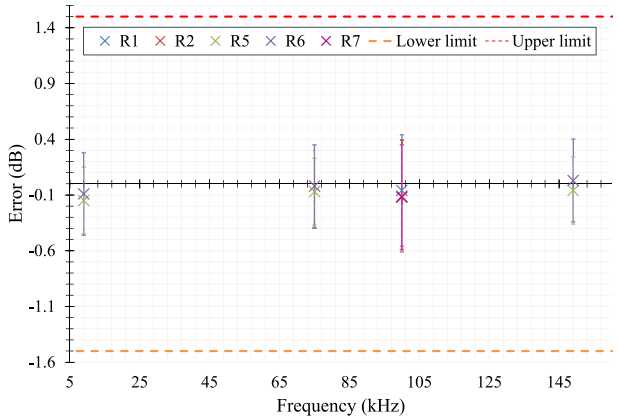


FIGURE 6. E0—CISPR Band A. Response to pulses. QP detector deviation at a pulse repetition frequency of 25 Hz. Absolute calibration.

Fig. 5 corresponds to the sinewave voltage level error in CISPR band B when a reference CW signal is fed to the receiver. Typically, the target amplitude level is 66 dBμV. For each receiver, the calibration points are plotted alongside error bars corresponding to the measurement uncertainty.

Next, we present some calibration results of the response to pulses. In Fig. 6, the focus is on the QP detector error when a pulsed signal at a reference repetition rate (25 Hz) is applied. On the other hand, Fig. 7 shows the error in the PK to quasi-peak ratio (PK/QP) at the said pulse repetition frequency (PRF). The absolute and the relative response to pulses are expected to be flat in a given CISPR band for a given PRF. For the reported cases, calibration points and the measurement uncertainty are indicated in the plots.

With respect to the resolution bandwidth (RBW) filter characteristics, Fig. 8 shows the 1.5, 6, and 20 dB decay points and the RBW filter mask requirement for band A. The standard does not fix the test frequency, so this is defined by the calibration laboratory. RBW filter characteristics are very similar in all the models considered in the analysis.

Data shows that direct sampling implementations do not perform differently (significantly better or worse)

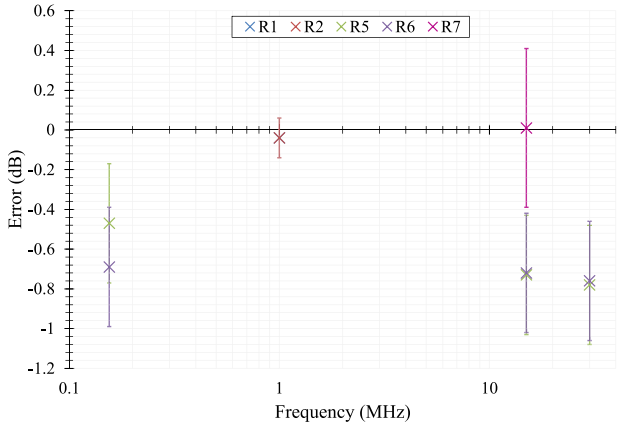


FIGURE 7. E0—CISPR Band B. Response to pulses. PK/QP ratio deviation at a pulse repetition frequency of 25 Hz.

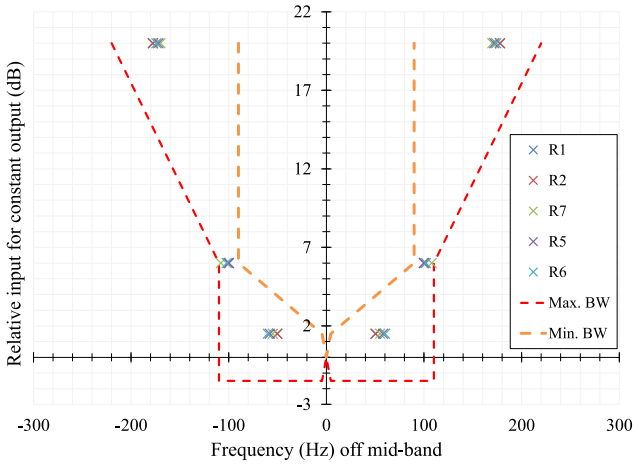


FIGURE 8. E0—CISPR Band A. Selectivity of the resolution bandwidth filter.

from receiver models using other architectures. The results for the bands or test conditions not shown above exhibit the same behavior and lead to equivalent conclusions.

B. PULSE MODULATED SINEWAVE

Figs. 9–11 show the error associated with the measurements obtained for each device, detector, and frequency under evaluation. It should be noted that the R2 data is not presented for the 500-MHz frequency due to the bandwidth limitations of the device.

The error limits of the graphs are between ±1.5 dB, as this is the CISPR 16-1-1 tolerance. No significant discrepancies were observed between the R3 and R4 errors and the oscilloscope-based implementations R1 and R2. In most cases, the error remains consistently within ±0.5 dB for all devices and detectors. The most prominent exception of this is exemplified in Fig. 11, at 100 and 500 MHz, where larger deviations in the average detector were found. In all cases, test results are within CISPR tolerance.

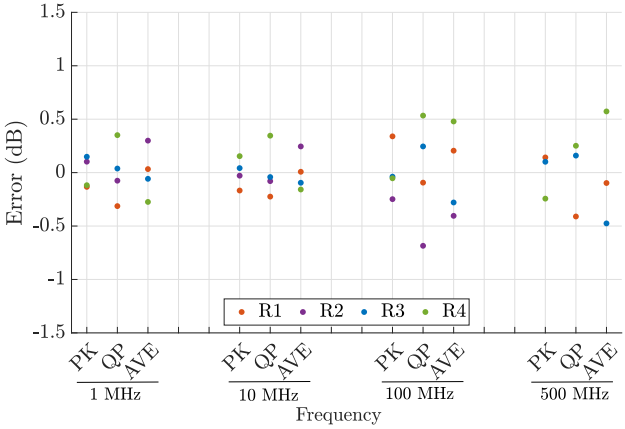


FIGURE 9. E1.1—Test condition: $\tau = 20\ \mu$s, $T = 1$ ms.

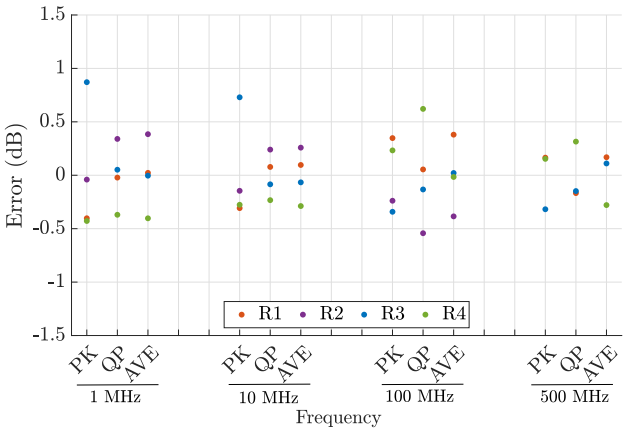


FIGURE 10. E1.1—Test condition: $\tau = 10\ \mu$s, $T = 100\ \mu$s.

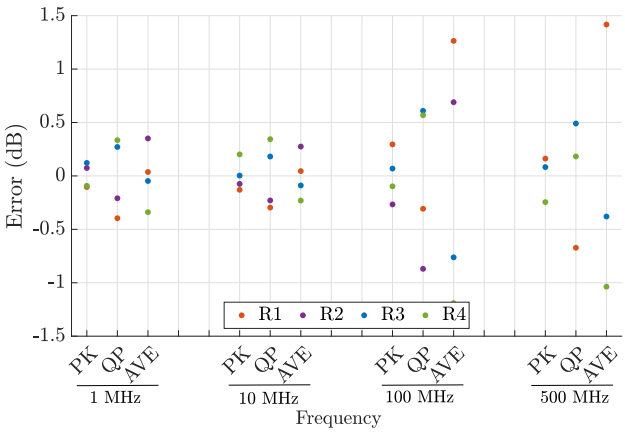


FIGURE 11. E1.1—Test condition: $\tau = 50\ \mu$s, $T = 1$ ms.

C. ALTERNATIVE GENERATED SIGNALS

In this section, first the noise level measurement results of the used receivers are presented, then results E1.2.3 and E1.2.5 are selected for demonstration as representing the most remarkable cases.

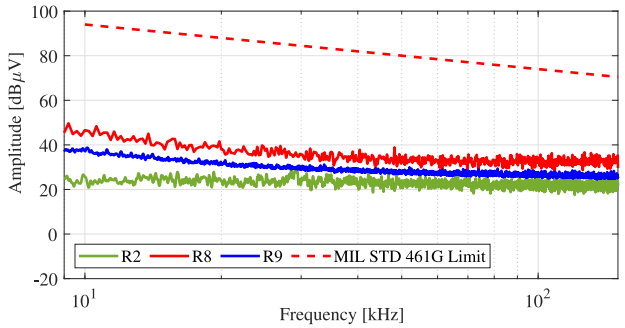


FIGURE 12. E1.2—Noise floor of the R2, R8, and R9 receivers.

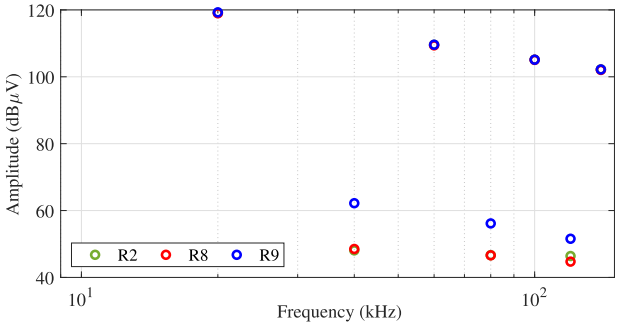


FIGURE 13. E1.2.3—Measurement results of the square signal. Peak detector.

1) NOISE LEVEL

Fig. 12 shows the noise floor of the receivers under test with the limit provided by MIL-STD 461G. All receivers perform noise level results at least 30 dB less than the limit line. The noise level of the R8 can be lower if the level of the used attenuator is reduced. However, this results in a lower measured voltage range. For consistency, Fig. 12 displays the noise level measurement results with uniform settings applied across all measurements.

2) SIGNALS WITH STABLE FREQUENCY CONTENT

In this section, the results of the three test signals with stable frequency content are reviewed together. For example, Fig. 13 presents the results of the square signal measurement via R2, R8, and R9 receivers at seven specific frequencies.

Since R8 is considered the reference device at this stage, within each pair (R2/R8 and R9/R8), the differences between their output at each specific frequency were found by

$$\Delta_{\mathrm{R2.j}} = S_{\mathrm{R8.j}} - S_{\mathrm{R2.j}} \tag{1}$$

$$\Delta_{\mathrm{R9.j}} = S_{\mathrm{R8.j}} - S_{\mathrm{R9.j}} \tag{2}$$

where $S_{\mathrm{R2.j}}$, $S_{\mathrm{R8.j}}$, and $S_{\mathrm{R9.j}}$ are the amplitude values measured via R2, R8, and R9 receivers at specific frequencies j.

Then, the maximum and average differences for each test signal and detector are found by

$$\Delta_{\mathrm{MAX.i}} = \max\left(\Delta_{ij}\right) \tag{3}$$

$$\Delta_{\mathrm{AVE.i}} = \mathrm{mean}\left(\Delta_{ij}\right) \tag{4}$$

where i corresponds to receivers under test.

Calculated Δ_{MAX} and Δ_{AVE} are listed in Table 6. As receiver R9 does not provide the average and quasi-peak detector, therefore R9 results are presented only for the peak detector. Within the E1.2.1 and E1.2.2 receivers, R2 and R9 show the results with a maximum deviation of 0.43 dB from reference receiver R8 for all detectors. In E1.2.3, the deviation becomes more significant, the average values in the R2/R8 pair increase up to 2 dB and the maximum deviation exceeds 3 dB for average and quasi-peak detectors. These significant deviations can be explained by the level of the measured signal at 120 kHz close to the noise level of the receivers used as can be seen in Fig. 13.

TABLE 6. E1.2—Maximum and average differences between receivers for the alternative signals with stable frequency content.

ID	Detector	R2/R8, (dB)		R9/R8, (dB)	
		Δ_{MAX}	Δ_{AVE}	Δ_{MAX}	Δ_{AVE}
E1.2.1	**PK**	0.08		0.08	
	AVE	0.08		-	
	QP	0.34		-	
E1.2.2	**PK**	0.14	-0.09	0.18	-0.09
	AVE	0.15	-0.10	-	
	QP	0.43	-0.37	-	
E1.2.3	**PK**	1.67	-0.26	13.69	-4.39
	AVE	4.35	-1.00	-	
	QP	4.47	-2.02	-	

3) SIGNALS WITH TIME-VARIANT FREQUENCY CONTENT

The measurement of time-variant signals needs to be analyzed over a spectrum of frequencies rather than at distinct ones. However, the data collected from different receivers can differ in length, even though they need to be uniform for effective cross-comparison. To achieve this, the results from R8 and R9 are linearly resampled to match the length of the R2 data set, ensuring the consistency of the original output behavior. For example, in Fig. 14, the resampled results of the chirp signal (E1.2.4) are presented. Although the set amplitude of the signal is 1 V_{RMS} (120 dBμV), all receivers resulted in lower values. It is the expected measurement result of the signal with the variant frequency content over the measurement time. The probability density function (PDF) and histogram clearly visualize the difference between the measurements received. They are presented in Fig. 15.

From Figs. 14 and 15, it is clear that R2 results in more close to R8 output in comparison to R9; only several 0.5 dB deeps are noticed. For these resampled data at the frequency range under interest (from 80 to 120 kHz), the differences within pairs R2/R8 and R9/R8 are found according to (1) and (2). The average difference ($\bar{d}$) and the standard deviation of differences (s_{d}) are defined, as well as the difference between the mode values (Δ_{MODE}) seen in Fig. 15.

Calculated values characterizing differences within pairs R2/R8 and R9/R8 for different detectors are presented in

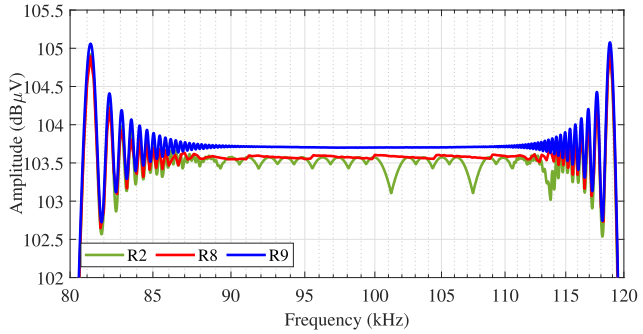


FIGURE 14. E1.2.4—Measurement results of the chirp signal.

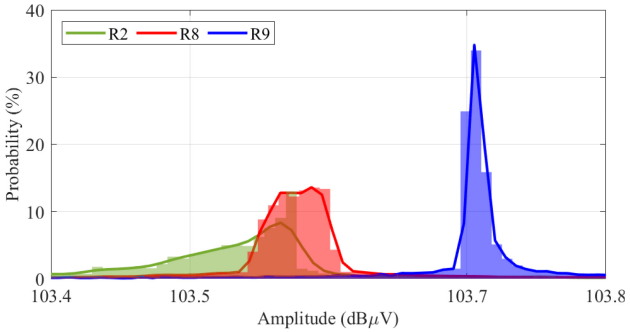


FIGURE 15. E1.2.4—The PDF of the chirp signal measurements.

TABLE 7. E1.2.4—Receivers comparison for the chirp signal.

Receiver	R9/R8	R2/R8		
Detector	PK	PK	AVE	QP
Δ_{MODE}, (dB)	-0.14	0.01	0.85	0.01
$\bar{d}$, (dB)	-0.14	0.07	-0.08	0.26
s_{d}, (dB)	0.05	0.11	1.13	0.31

Table 7. Average differences over the frequency range of interest are much lower than 3 dB for all detectors. The mode value of the R8 and R2 results differs by 0.01 dB. Oppositely, R9 results in a mode value 0.14 dB dB higher. The low value of the s_d indicates that R9 results are consistently higher than R2 results throughout the frequency range.

The spectrum measurement of the E1.2.5 has four characteristic frequency spans, as shown in Fig. 16. Each frequency span is processed separately in the same way as for the chirp signal above.

The differences in peak detector measurements in R2/R8 and R9/R8 pairs are found, and for the R2/R8 pair, the results of the average and quasipeak detectors are compared and analyzed. Then, the maximum and average differences over four spans are found. Table 8 summarizes the average values that characterize the differences between R2 and R9 measurements from R8. Average and maximum deviations between measurements, as well as standard deviation, show the high accuracy of using R2 receiver. The calculated deviations are in the range of ±1 dB.

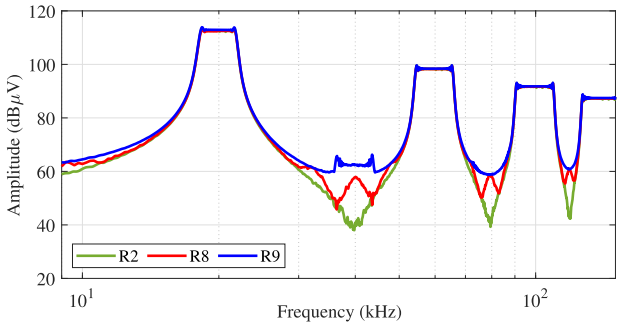


FIGURE 16. E1.2.5—Square signal with variant modulated frequency measurements. Peak detector.

TABLE 8. E1.2.5—Receivers comparison for the square signal with variant modulated frequency.

Receiver	R9/R8	R2/R8		
Detector	PK	PK	AVE	QP
Δ_{MODE}, (dB)	-0.19	-0.08	0.59	-0.12
$\bar{d}$, (dB)	-0.26	-0.05	-0.06	-0.30
s_{d}, (dB)	0.11	0.15	1.01	0.32

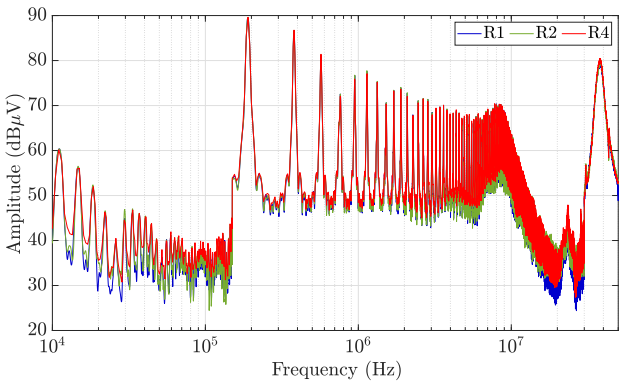


FIGURE 17. E2.1—Conducted emissions, positive line (LISN OUT 0).

D. EMISSIONS OF COST DC/DC CONVERTER

The results of this experiment are structured according to the most relevant observations made during the data analysis stage, including considerations about harmonic voltage level accuracy, broadband voltage level accuracy, resonances, and noise floor. In particular, Fig. 17 shows the spectrum comparison between the R1, R2, and R4 for the positive line (OUT 0) of the LISN, and this case is used to exemplify the general observations.

1) HARMONIC VOLTAGE LEVEL ACCURACY

Figs. 18–20 show R4 delivers a coarser frequency resolution than R1 and R2 for the same basic settings. This might be explained by the type of frequency interpolation used, including the interpolation ratios and algorithms. R1 and R2 use the Akima method, while R4 applies linear interpolation.

2) BROADBAND VOLTAGE LEVEL ACCURACY

Fig. 21 shows the broadband emission spectrum measured when the resolution bandwidth is larger than the distance

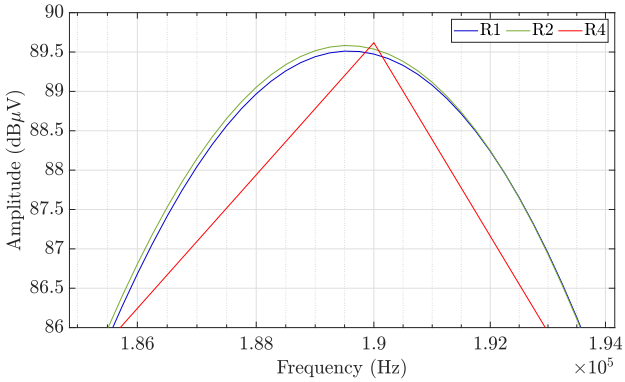


FIGURE 18. E2.1—Zoom of harmonic at 189 kHz.

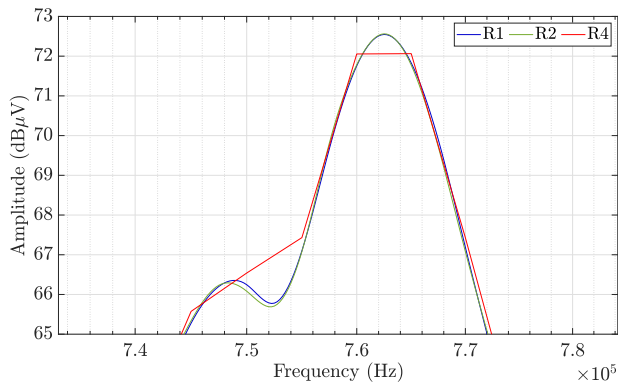


FIGURE 19. E2.1—Zoom of harmonic at 762.5 kHz.

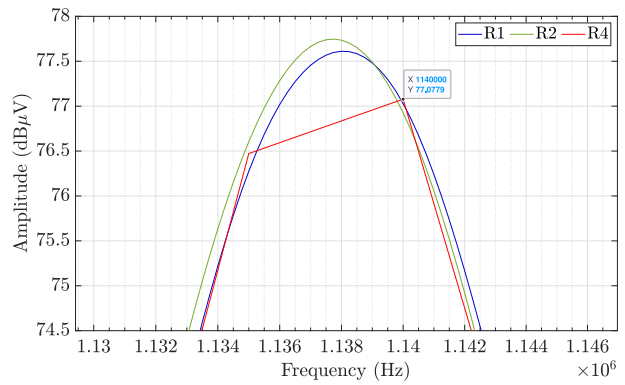


FIGURE 20. E2.1—Zoom of harmonic at 1.138 MHz.

between individual harmonic components. An excellent agreement is observed in the spectrum amplitude for all receivers considered. To quantify the difference between R4 (reference) and the oscilloscope-based systems (R1 and R2), the deviations are calculated as

$$\overline{\Delta_1} = S_{R4} - S_{R1} \tag{5}$$

$$\overline{\Delta_2} = S_{R4} - S_{R2}. \tag{6}$$

Fig. 22 compares the approximated distribution of the deviations in (5) and (6) using a histogram format. The mean values of the calculated errors in that frequency range $\overline{\Delta_1}$ and $\overline{\Delta_2}$ are very close to 0 dB, being −0.16 and 0.06 dB, respectively.

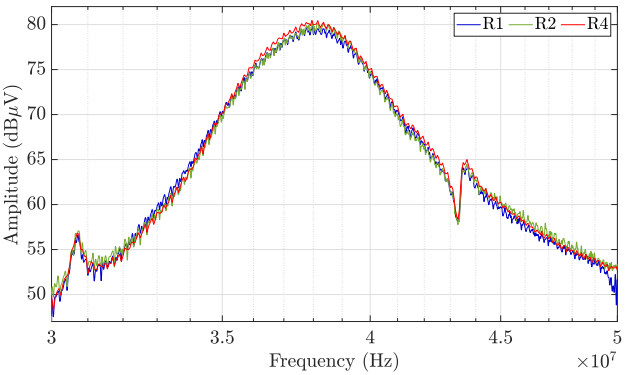


FIGURE 21. E2.1—Broadband emissions in the range 30–50 MHz.

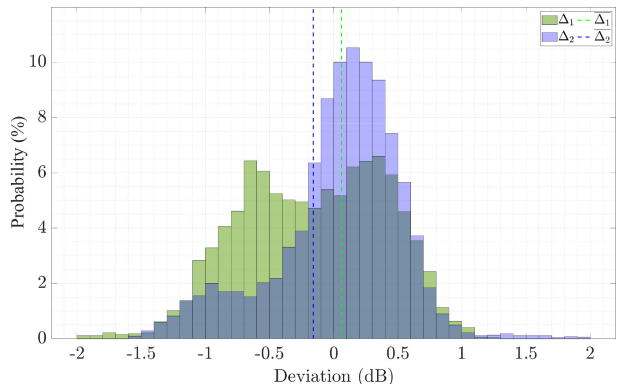


FIGURE 22. E2.1—Difference in the amplitude levels for broadband emissions in the range 30–50 MHz.

TABLE 9. E2.1—Analysis at the resonance frequencies.

	R1	R2	R4	R1	R2	R4
Level, (dBμV)	57.07	56.62	56.77	57.76	58.21	58.37
Frequency, (MHz)	30.74	30.72	30.70	43.29	43.31	43.33

3) RESONANCES

Around resonances, the spectrum amplitude changes rapidly with frequency. In this case, some examples of small resonances are found in Fig. 21. Table 9 shows the amplitude level and frequency of both resonance peaks. In those two cases, we found less than 0.5 dB and 40 kHz of difference.

4) NOISE FLOOR

Fig. 23 shows the noise floor of R1, R2, and R4 compared with a conducted emissions limit; in this case, we used the limit corresponding to the CE102 test according to the MIL-STD-461G. According to the data, noise levels are sufficiently low. However, we found out that R4 in its by intended configuration (without preamplifier and with 10 dB of internal attenuation) delivered the higher noise floor.

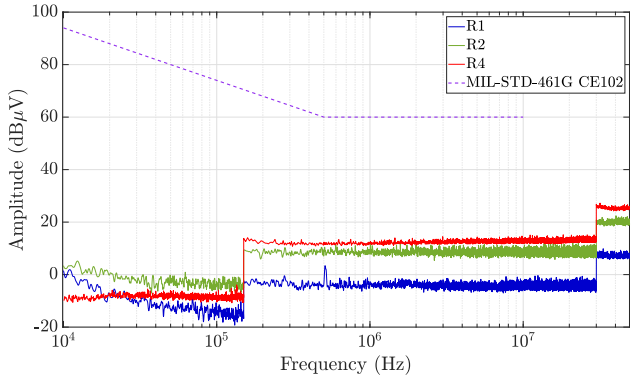


FIGURE 23. Noise floor and standard limit comparison.

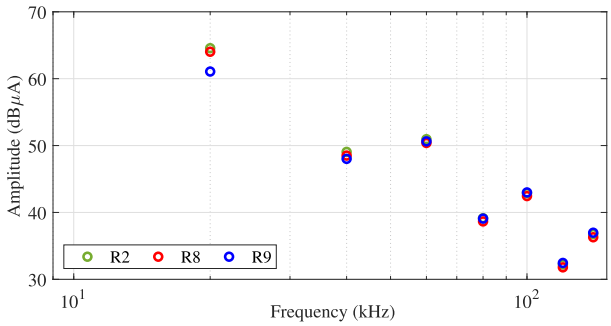


FIGURE 24. E2.2.1—Continuous PWM. Peak detector.

E. EMISSIONS OF DC/DC CONVERTER USING SPREAD SPECTRUM MODULATION

The results of the EMI measurements of the dc/dc GaN converter with different PWM are presented in this section. In this case, the EMI is presented via normal mode current I_{NM}, and its measurements are performed via an RF current probe.

1) CONTINUOUS PULSE WIDTH MODULATION

The continuous PWM with a fundamental frequency of 20 kHz applied for the dc/dc GaN converter resulted in EMI with seven specific frequencies below 150 kHz, similar to the spectrum of the square signal, presented in Fig. 13. In Fig. 24, the measurement results of the peak detector are presented. The deviations of the R2 and R9 output from R8 measurements are defined by (1) and (2). The maximum and average deviations for the three detectors are listed in Table 10.

The receiver R2 results in a uniform deviation from the reference R8 output for all detectors in the range between 0.43 and 0.7 dB. Meanwhile, R9 results in a higher deviation from R2 by up to 2.96 dB at 20 kHz.

2) SPREAD SPECTRUM PULSE WIDTH MODULATION

A spread spectrum technique is used to reduce the emission detected in the standard emission tests, as it can be seen in Fig. 25, where the results of the I_{NM} measurements of the converter controlled with random spread spectrum PWM using the peak detector are presented. In contrast

TABLE 10. E2.2.1—Receivers comparison for the EMI from the converter controlled with continuous PWM.

Detector	R2/R8		R9/R8	
	Δ_{MAX}, (dB)	Δ_{AVE}, (dB)	Δ_{MAX}, (dB)	Δ_{AVE}, (dB)
PK	-0.43	-0.49	2.96	0.13
AV	-0.43	-0.50	-	
QP	-0.70	-0.77	-	

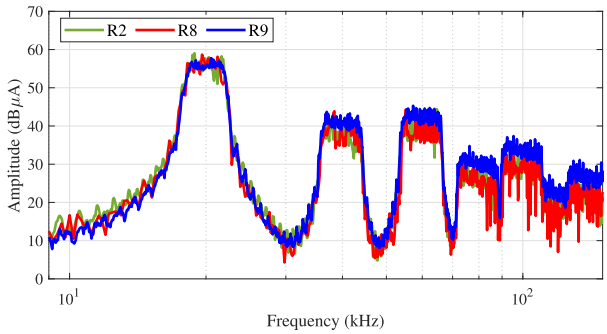


FIGURE 25. E2.2.3—The EMI from the converter controlled with random spread spectrum PWM.

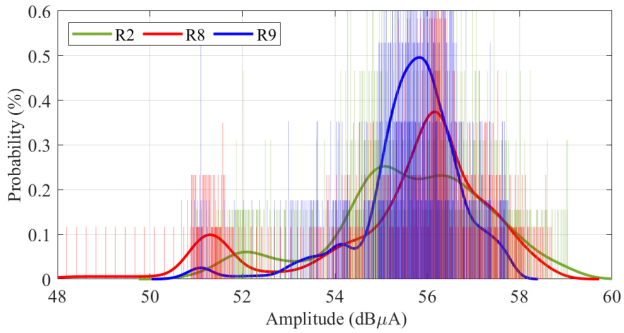


FIGURE 26. E2.2.3—The PDF of the EMI from the converter controlled with random spread spectrum PWM.

to the square signal in Fig. 16, here six specific frequency ranges can be highlighted. In Fig. 25, a high number of peaks and dips over the frequency under study are clearly seen. The I_{NM} of the dc/dc GaN converted controlled by random spread spectrum PWM is the most complex time-variant EMI within the framework of this article. However, as can be seen in Fig. 26, the PDF for the first frequency range from 18 to 22 kHz shows very similar results for peak detectors of the receivers under study.

For both results of the E2.2.2 and E2.2.3, the analyses similar to the one used for the generated signals with time-variant frequency content are performed and listed in Tables 11 and 12, respectively. The E2.2.2 results in the average deviation from the R2 output is less than 2 dB, for all detectors. The standard deviations are up to 1.17 dB. Meanwhile, for the emission from the dc/dc converter with random spread spectrum PWM, despite the measured signal's complexity, the R2 results' average deviation for all detectors is within 3 dB. It is also quite remarkable that the

TABLE 11. E2.2.2—Receivers comparison for the EMI from the converter with linear spread spectrum PWM. Average deviations from R8.

Receiver	R9/R8	R2/R8		
Detector	PK	PK	AVE	QP
Δ_{MODE}, (dB)	-0.99	-1.24	-1.30	-2.22
$\overline{d}$, (dB)	-1.21	-1.09	-1.09	-1.63
s_d, (dB)	0.45	0.43	1.17	0.55

TABLE 12. E2.2.3—Receivers comparison for the EMI from the converter with random spread spectrum PWM. Average deviations from R8.

Receiver	R9/R8	R2/R8		
Detector	PK	PK	AVE	QP
Δ_{MODE}, (dB)	-2.49	-1.42	1.04	-2.45
$\overline{d}$, (dB)	-2.63	-1.40	0.54	-2.44
s_d, (dB)	2.53	2.72	2.80	1.53

differences between R9 and R8 are slightly larger than in pair R2/R8.

V. CONCLUSION

Previous works have verified the performance of time-domain measuring receivers based on direct sampling instruments. However, the corresponding evidence remained scattered and focused either on calibration data or specific use cases. This study bridged that gap by providing a sequence of validations through a multilevel approach. In five different experiments, commercial EMI receivers (frequency-swept and FFT-based) were compared with an oscilloscope-based counterpart (R1 and R2) following an approach where the complexity of the excitation signals increased progressively.

Based on the results obtained, it is concluded that R1 and R2 performed as well as their CISPR 16-1-1 compliant counterparts in the frequency and amplitude ranges evaluated; that is, the measurement errors in various test conditions remained well within standard tolerances. It is essential to recall that this is the first work where such multilevel and extensive empirical validation has been explicitly carried out, in collaboration with independent teams, to benchmark direct sampling implementations of FFT-based measuring receivers with commercial solutions.

The robustness of the work is grounded in the combined representativeness of the different scenarios and the size of the test sample used. Because of page length restrictions and for the sake of conciseness, this article presents only a subset of representative results to support our claims. In all cases, the authors commit to sharing the complete measurement data upon request for those interested.

We expect this work will contribute to leveraging EMC standardization by supporting the explicit mention of EMI receivers based on direct sampling instruments. Widening the measuring receiver definition in this way would open up a broad range of possibilities for new measurement setups based on multichannel and full time-domain capabilities. Such features, previously exploited in research projects, bring advantages that are called for widespread applications in the practice of EMC.

REFERENCES

[1] *Specification for Radio Disturbance and Immunity Measuring Apparatus and Methods—Part 1-1: Radio Disturbance and Immunity Measuring Apparatus—Measuring Apparatus*, IEC Standard CISPR 16-1-1:2019 ed 5.0, Jun. 2019.

[2] M. Pous, D. Zhao, M. A. Azpúrua, T. Bozhanov, F. Silva, and J. Wolf, "Time-domain electromagnetic characterization of reaction wheel for space applications," *IEEE Trans. Electromagn. Compat.*, vol. 65, no. 2, pp. 365–375, Apr. 2023.

[3] K. Pliakostathis, M. Zanni, G. Trentadue, and H. Scholz, "Vehicle electromagnetic emissions: Challenges and considerations," in *Proc. Int. Symp. Electromagn. Compat. (EMC EUROPE)*, 2019, pp. 1106–1111.

[4] R. Gamoudi, D. E. Chariag, and L. Sbita, "A review of spread-spectrum-based PWM techniques—A novel fast digital implementation," *IEEE Trans. Power Electron.*, vol. 33, no. 12, pp. 10292–10307, Dec. 2018.

[5] P. Russer, "EMC measurements in the time-domain," in *Proc. 30th URSI General Assem. Sci. Symp.*, 2011, pp. 1–35.

[6] J. Solé-Lloveras, M. A. Azpúrua, Y. Yoshioka, and F. Silva, "Strategies using time-domain measurements for radiated emissions testing in harsh environments," *IEEE Open J. Instrum. Meas.*, vol. 2, pp. 1–11, Aug. 2023.

[7] J. Solé-Lloveras, M. A. Azpúrua, M. A. Homar, Y. Yoshioka, and F. Silva, "Efficient in situ assessment of radiated emissions using time-domain measurements," in *Proc. Int. Symp. Electromagn. Compat. (EMC Europe)*, 2023, pp. 1–6.

[8] M. Pous, M. Azpúrua, and F. Silva, "Benefits of full time-domain EMI measurements for large fixed installation," in *Proc. Int. Symp. Electromagn. Compat. (EMC EUROPE)*, 2016, pp. 514–519.

[9] M. Pous, M. A. Azpúrua, J. A. Oliva, M. Aragón, I. González, and F. Silva, "Full time domain EMI measurement system applied to railway emissions according to IEC 62236-3-1/EN 50121-3-1 standards," in *Proc. Int. Symp. Electromagn. Compat. (EMC EUROPE)*, 2018, pp. 260–265.

[10] D. Pokotilov, R. Vogt-Ardatjew, and F. Leferink, "Efficient multichannel time-domain multiaxis loop antenna measurement for frequencies below 30 MHz," in *Proc. IEEE Int. Joint EMC/SI/PI EMC Europe Symp.*, 2021, pp. 648–652.

[11] F. Krug and P. Russer, "The time-domain electromagnetic interference measurement system," *IEEE Trans. Electromagn. Compat.*, vol. 45, no. 2, pp. 330–338, May 2003.

[12] F. Krug, D. Mueller, and P. Russer, "Signal processing strategies with the TDEMI measurement system," *IEEE Trans. Instrum. Meas.*, vol. 53, no. 5, pp. 1402–1408, Oct. 2004.

[13] F. Krug and P. Russer, "Quasi-peak detector model for a time-domain measurement system," *IEEE Trans. Electromagn. Compat.*, vol. 47, no. 2, pp. 320–326, May 2005.

[14] S. Braun, T. Donauer, and P. Russer, "A real-time time-domain EMI measurement system for full-compliance measurements according to CISPR 16-1-1," *IEEE Trans. Electromagn. Compat.*, vol. 50, no. 2, pp. 259–267, May 2008.

[15] S. Braun, C. Hoffmann, A. Frech, and P. Russer, "A realtime time-domain EMI measurement system for measurements above 1 GHz," in *Proc. IEEE Int. Symp. Electromagn. Compat.*, 2009, pp. 143–146.

[16] S. Braun, "A novel time-domain EMI measurement system for measurement and evaluation of discontinuous disturbance according to CISPR 14 and CISPR 16," in *Proc. IEEE Int. Symp. Electromagn. Compat.*, 2011, pp. 480–483.

[17] C. Hoffmann, A. Sidhom, S. Braun, and P. Russer, "A broadband, low-noise time-domain system for EMI measurements through Ka-band up to 40 GHz," in *Proc. IEEE Int. Symp. Electromagn. Compat.*, 2012, pp. 468–472.

[18] M. A. Azpúúrua, M. Pous, S. Çakir, M. Çetinta, and F. Silva, "Improving time-domain EMI measurements through digital signal processing," *IEEE Electromagn. Compat. Mag.*, vol. 4, no. 2, pp. 82–91, 2nd Quart., 2015.

[19] M. Pous and F. Silva, "Full-spectrum APD measurement of transient interferences in time domain," *IEEE Trans. Electromagn. Compat.*, vol. 56, no. 6, pp. 1352–1360, Dec. 2014.

[20] M. A. Azpúúrua, M. Pous, and F. Silva, "On the statistical properties of the peak detection for time-domain EMI measurements," *IEEE Trans. Electromagn. Compat.*, vol. 57, no. 6, pp. 1374–1381, Dec. 2015.

[21] M. A. Azpúúrua, M. Pous, and F. Silva, "Decomposition of electromagnetic interferences in the time-domain," *IEEE Trans. Electromagn. Compat.*, vol. 58, no. 2, pp. 385–392, Apr. 2016.
[22] T. Hartman, N. Moonen, and F. Leferink, "Direct sampling in multichannel synchronous TDEMI measurements," in *Proc. IEEE 4th Glob. Electromagn. Compat. Conf. (GEMCCON)*, 2018, pp. 1–5.
[23] T. Hartman, R. Grootjans, N. Moonen, and F. Leferink, "Time-domain EMI measurements using a low cost Digitizer to Optimize the total measurement time for a test receiver," in *Proc. Int. Symp. Electromagn. Compat. (EMC EUROPE)*, 2020, pp. 1–6.
[24] B. T. Have et al., "Waveform model to characterize time-domain pulses resulting in EMI on static energy meters," *IEEE Trans. Electromagn. Compat.*, vol. 63, no. 5, pp. 1542–1549, Oct. 2021.
[25] M. Hudlička, M. A. Azpúrua, and M. Wojciechowski, "Metrological characterization of EMI receivers," in *Proc. Int. Symp. Electromagn. Compat. (EMC Europe)*, 2023, pp. 1–6.
[26] M. A. Azpúrua, M. Pous, J. A. Oliva, B. Pinter, M. Hudlička, and F. Silva, "Waveform approach for assessing conformity of CISPR 16-1-1 measuring receivers," *IEEE Trans. Instrum. Meas.*, vol. 67, no. 5, pp. 1187–1198, May 2018.
[27] M. A. Azpúrua, M. Pous, M. Fernandez, and F. Silva, "Dynamic performance evaluation of full time domain EMI measurement systems," in *Proc. Int. Symp. Electromagn. Compat. (EMC EUROPE)*, 2018, pp. 561–566.
[28] M. A. Azpúrua, M. Pous, and F. Silva, "Statistical evaluation of measurement accuracy in full time-domain EMI measurement systems," in *Proc. Int. Symp. Electromagn. Compat. (EMC EUROPE)*, 2020, pp. 1–6.
[29] M. García-Bermúdez, J. Solé-Lloveras, M. Hudlička, and M. A. Azpúrua, "Evaluation of spectral estimation parameters for direct sampling FFT-based measuring receivers," *IEEE Open J. Signal Process.*, vol. 5, pp. 588–598, Apr. 2024.



IVAN STRUZHKO (Member, IEEE) received the B.Sc. degree in electrical engineering and the M.Sc. degree in electrical power engineering, electrical engineering, and electromechanics from Pryazovskyi State Technical University, Dnipro, Ukraine, in 2013 and 2015, respectively. He is currently pursuing the Ph.D. degree in electromagnetic compatibility with the Power Electronics and Electromagnetic Compatibility Group, University of Twente, Enschede, The Netherlands.

Since then, he has worked as an Electric and Power Energy Engineer with the Armavirskiy Machine Building Plant, Armavir, Russia, and a Teaching Assistant with the Department of Electrical Engineering, Pryazovskyi State Technical University. His research interest is focused on the implementation of the cognitive radio concept for the EMC applications.



MARC GARCÍA-BERMÚDEZ received the B.Sc. degree in electronic engineering and telecommunications from the Universitat Politècnica de Catalunya, Barcelona, Spain, in 2024, and the master's degree in aerospace science and technology from the Universitat Politècnica de Catalunya, Barcelona, Spain, in 2025.

He is currently a Research Intern with EMC Barcelona, Barcelona, actively supporting the 21NRM06 Project "Metrology for Emerging Electromagnetic Compatibility Standards" and the company activities as incubatees of the ESA Business Incubation Center in Barcelona.



JORDI SOLÉ-LLOVERAS (Member, IEEE) received the B.Sc. degree in telecommunication engineering and the M.Sc. degree in electronics engineering from the Universitat Politècnica de Catalunya (UPC), Barcelona, Spain, in 2020 and 2022, respectively, where he is currently pursuing the Ph.D. degree with research focused on in situ emissions assessments of large systems.

Since 2018, he has been part of the Grup de Compatibilitat Electromagnètica, UPC, where he has been involved in testing and technology transfer projects. Since 2021, he has been working with EMC Barcelona, Barcelona, where he participates in research and development and consultancy projects.



MANUEL AÑÓN-CANCELA received the M.Sc. degree in physics from the Universidade de Santiago de Compostela, Santiago, Spain, in 1989.

In 1991, he joined INTA, Madrid, Spain, as an E3 Test Engineer in the Electromagnetic Compatibility Area, being involved in several national and international projects for the aerospace and defense sectors. He is currently the Head of the EMC Area, INTA. He is a member of national and international standardization groups for military and civilian E3 specs.



TOM HARTMAN (Member, IEEE) received the B.Sc. degree in electrical engineering, the M.Sc. degree in electrical engineering, and the Ph.D. degree (cum laude) in EMC from the University of Twente, Enschede, The Netherlands, in 2016, 2018, and 2023, respectively.

He is currently working as an Assistant Professor with the University of Twente.

Dr. Hartman had the honor of receiving the 2021 President Memorial Award of the IEEE EMC Society and the 2022 Richard B. Shultz Best Transaction Paper Award of IEEE Transactions on Electromagnetic Compatibility for the journal paper titled: "Susceptibility of Static Energy Meters Due to Amplifier Clipping Caused by a Rogowski Coil."



MARCO A. AZPÚRUA (Senior Member, IEEE) received the B.Sc. degree in telecommunications and the M.Sc. degree in electrical engineering from the Universidad Central de Venezuela, Caracas, Venezuela, in 2008 and 2013, respectively, and the Ph.D. degree in electronics engineering from the Universitat Politècnica de Catalunya (UPC), Barcelona, Spain, in 2018.

He currently works as an Associate Professor with the Electronic Engineering Department, UPC, where he is part of the EMC Group. He is the Co-Founder of EMC Barcelona and a Fellow of the StandICT.eu projects (2023 and 2026).

Dr. Azpúrua is a member of the CISPR/CIS/B/WG 1 and WG 7, the IEEE EMC and IMS societies, and the IEEE/ICES.



FRANK LEFERINK (Fellow, IEEE) received the B.Sc., M.Sc., and Ph.D. degrees in electrical engineering from the University of Twente, Enschede, The Netherlands, in 1984, 1992, and 2001, respectively.

Since 1984, he has been with THALES, Hengelo, The Netherlands, where he is currently the Director of EMC. He is also a Manager of the Network of Excellence on EMC, THALES Group, with more than 100 EMC engineers scattered over more than 20 units, worldwide. In 2003, he joined as a (part-time, full research) Professor and holds the Chair for EMC with the University of Twente. He has authored and co-authored more than 300 papers published at international conferences or peer-reviewed journals, and he holds five patents.

Prof. Leferink is the past President of the Dutch EMC-ESD Association, the Chair of the IEEE EMC Benelux Chapter, a member of ISC EMC Europe, the Chairman of EMC Europe 2018 (Amsterdam, The Netherlands), a member of the Board of Directors of the IEEE EMC Society, and an Associate Editor of the IEEE TRANSACTIONS ON ELECTROMAGNETIC COMPATIBILITY and the IEEE LETTERS ON ELECTROMAGNETIC COMPATIBILITY PRACTICE AND APPLICATIONS.